Backscatter 2-μm Lidar Validation for Atmospheric CO_2 Differential Absorption Lidar Applications

Tamer F. Refaat, *Member, IEEE*, Syed Ismail, Grady J. Koch, Manuel Rubio, Terry L. Mack, Anthony Notari, James E. Collins, Jasper Lewis, Russell De Young, Yonghoon Choi, M. Nurul Abedin, *Member, IEEE*, and Upendra N. Singh

***Abstract*—A 2-μm backscatter lidar system has been developed by utilizing tunable pulsed laser and infrared phototransistor for the transmitter and the receiver, respectively. To validate the system, the 2-μm atmospheric backscatter profiles were compared to profiles obtained at 1 and 0.5 μm using avalanche photodiode and photomultiplier tube, respectively. Consequently, a methodology is proposed to compare the performance of different lidar systems operating at different wavelengths through various detection technologies. The methodology is based on extracting the system equivalent detectivity and comparing it to that of the detectors, as well as the ideal background detectivity. Besides, the 2-μm system capability for atmospheric CO_2 temporal profiling using the differential absorption lidar (DIAL) technique was demonstrated. This was achieved by tuning the laser at slightly different wavelengths around the CO_2 R22 absorption line in the 2.05-μm band. CO_2 temporal profiles were also compared to *in situ* measurements. Preliminary results indicated average mixing ratios close to 390 ppm in the atmospheric boundary layer with 3.0% precision. The development of this system is an initial step for developing a high-resolution, high-precision direct-detection atmospheric CO_2 DIAL system. A successful development of this system would be a valuable tool in obtaining and validating global atmospheric CO_2 measurements.**

***Index Terms*—Backscattering, carbon dioxide, infrared, lidar, remote sensing.**

I. Introduction

LIDAR is an important tool for profiling atmospheric aerosols, clouds, and molecular species distributions [1]. Unlike the ultraviolet (UV) and visible regions, infrared lidars provide the potential for increasing the transmitted laser energy while maintaining eye-safety requirements, which allows for longer operating range with higher sensitivities [2], [3]. As a consequence, sophisticated lidar methodology, such as the differential absorption lidar (DIAL), could be applied in this region. This allows addressing important issues, including the study of the atmospheric radiative effect and climate change on Earth. Lidar systems operating at 2 μm are of special interest due to its many distinctive absorption features for important atmospheric constituents, such as water vapor and carbon dioxide [3], [4]. Thus, extensive research efforts are focused on developing new technologies at this particular wavelength. For example, under NASA programs, different components were developed, including advanced 2 μm tunable pulsed lasers and optical detectors, providing the motivation for developing an atmospheric CO_2 DIAL system [5]–[7].

A backscatter lidar system operating at 2 μm was demonstrated by Sugimoto *et al.* [2]. The group profiled aerosol density and estimated the atmospheric volume backscatter coefficient at this wavelength. Using the same system, atmospheric water vapor was profiled using the DIAL technique [4]. Several studies were conducted for measuring atmospheric carbon dioxide using direct-detection DIAL [3], [8]–[10]. Such systems would provide valuable tools for validating satellite-based systems, such as the greenhouse gas observing satellite (GOSAT), and future active and passive satellite systems which aid in studying the sources and sinks of the carbon cycle [11], [12]. Generally, studies of CO_2 DIAL systems focus on both 1.6- and 2.0-μm wavelengths [3], [8]. CO_2 DIAL systems operating at 1.6 μm provide acceptable sensitivity where enhanced detector technology exists, such as InGaAs avalanche photodiodes (APD) and photomultiplier tubes (PMT). At this wavelength, Sakaizawa *et al.* developed a CO_2 DIAL profiling system with a precision of 1% [9]. This team utilized an IR PMT operating in a photon counting mode (Hamamatsu H10330-75). On the other hand, better CO_2 measurement sensitivity would be achievable through systems operating at 2 μm, which is due to more than one order of magnitude stronger absorption lines at this particular wavelength compared to 1.6 μm. Nevertheless, CO_2 DIAL systems operating at 2 μm face a significant challenge due to the limited availability of high performance quantum detectors operating at this wavelength. Uchiumi *et al.* reported a 2-μm CO_2 DIAL system with an InGaAs pin detector [10]. This resulted in a poor DIAL performance due to detector sensitivity limitations. To avoid detector limitations, 2-μm DIAL systems using heterodyne detection have been developed [13], [14]. Applying coherent detection overcomes the lack of photodiode sensitivity at this wavelength. However, the drawback of coherent heterodyne detection includes the speckle noise that limits the precision of the DIAL system and increased complexity and cost for space-based systems [13], [14]. Thus, direct detection designs using high sensitivity photodetectors are desired.

Manuscript received September 22, 2009; revised April 15, 2010; accepted May 31, 2010. Date of publication August 30, 2010; date of current version December 27, 2010. This work was supported in part by the NASA Instrument Incubator Program and in part by the NASA Laser Risk Reduction Program.

T. F. Refaat is with the Applied Research Center, Old Dominion University, Newport News, VA 23606 USA (e-mail: trefaat@odu.edu).

S. Ismail, G. J. Koch, M. Rubio, R. De Young, M. N. Abedin and U. N. Singh are with the NASA Langley Research Center, Hampton, VA 23681 USA.

T. L. Mack is with Lockheed Martin, Hampton, VA 23681 USA.

A. Notari and J. E. Collins are with Science Systems & Application, Inc., Hampton, VA 23681 USA.

J. Lewis and Y. Choi are with National Institute of Aerospace, Hampton, VA 23681 USA.

Color versions of one or more of the figures in this paper are available online at http://ieeexplore.ieee.org.

Digital Object Identifier 10.1109/TGRS.2010.2055874

0196-2892/$26.00 © 2010 IEEE

Authorized licensed use limited to: University of North Texas. Downloaded on December 18,2020 at 12:58:59 UTC from IEEE Xplore. Restrictions apply.

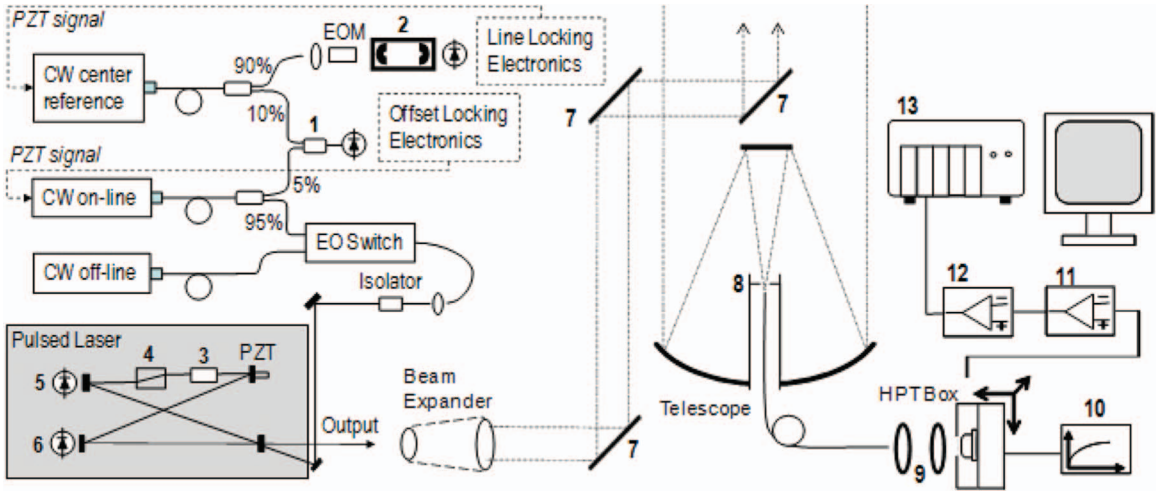

Fig. 1. Schematic diagram of the 2-μm lidar system. The main components of the 90-mJ, 140-ns, 5-Hz pulsed Ho:Tm:LuLiF laser transmitter are (1) evanescent wave fiber optic coupler, (2) CO_2 gas cell for wavelength center, (3) the laser rod, (4) acosto-optic Q-switch, (5) output pulse timing and energy monitor, and (6) injection seed resonance monitor. The output laser beam is expanded and transmitted coaxially with the receiver telescope using folding mirrors (7). The collected backscatter radiation is focused into a fiber through a pinhole (8) to limit the FOV. Aft-optics (9) focuses the radiation onto the HPT. The HPT temperature is set using a temperature controller (10), while the output is applied to trans-impedance amplifier (11) and voltage amplifier (12), before being digitized by the system digitizer (13).

Newly developed Sb-based hetero junction phototransistors (HPT) operating at 2-μm wavelength provide a solution for the detector sensitivity problem [6]. These detectors exhibit a high internal gain that leads to increased signal-to-noise ratio (SNR) making it attractive for 2-μm DIAL application [6]. Other HPT advantages include high quantum efficiency and small sensitive area. Quantum efficiency measurements indicated a peak around 2 μm, with sensitivity in the 1 to 2.2-μm region. The spectral sensitivity range tends to reduce the background signal, while the small sensitive area (200 μm diameter) reduces the device noise. Recently, such devices were validated for lidar applications at 1.6 μm in comparison with InGaAs APDs [15], [16]. Results indicated that incorporating such devices in lidar introduces blurring to the backscattered signals in the form of longer settling time. The longer settling time is a result of bandwidth limitation that affects the system resolution. Implementing deconvolution algorithm recovers the system resolution while reducing the SNR. This was achieved by experimentally measuring the lidar detection system transfer function and applying it to correct the lidar data in time-domain by iterative deconvolution [16]. In this paper, a 2-μm lidar system utilizing the HPT as a detector is presented. The new system is validated by comparison with the compact aerosol lidar (CAL) operating at 532 and 1064 nm [17], [18]. The comparison will focus generally on the lidar performance and specifically on different detection technologies, in the form of PMT, APD, and HPT for 532, 1064, and 2053 nm detection, respectively. Also, the capability of the 2-μm lidar to capture atmospheric CO_2 temporal profiles is demonstrated.

II. Two-Micron Backscatter Lidar Setup

The 2-μm backscatter lidar system was constructed at the NASA Langley Research Center (LaRC), Hampton, VA. Fig. 1 shows a schematic of the system, which was integrated inside an environmentally conditioned trailer. The trailer gives portability to the system for deployment in different validation sites. A window installed on the trailer roof allows operation of the lidar in the zenith mode. For validation purposes, the CAL aerosol lidar was located about 1.6 km away and was operated independently and simultaneously with the 2-μm lidar system.

The CAL can be pointed in the zenith for ground-based measurements or in the nadir for aircraft-based measurements. The CAL transmitter consists of a frequency doubled Nd:YAG laser with a 20-Hz pulse repetition rate. The laser transmits both 532- and 1064-nm beams in a biaxial configuration with the receiver telescope. The system receiver employs a 28-cm diameter telescope with a 2-mrad field-of-view (FOV). The received radiation is collimated and split into 1064- and 532-nm channels, with a further split of the 532-nm signal into analog (90%) and photon counting (10%) channels. The 1064-nm return passes through a 1-nm filter before being focused onto a Si APD (Perkin-Elmer C30955E) detector. The 532-nm return passes through a 0.5-nm filter before being split between analog and photon-counting photomultiplier detectors. Both the analog and photon counting channels utilize a microchannel PMT (Perkin-Elmer MH-943 and MP-943 modules, respectively). The APD and analog PMT outputs are amplified and conditioned before digitization by a 14-bit, 5-MS/s waveform analyzer (Gage Applied Inc. #1450). Default signal processing of the data includes 40 shots average (2 s) of the collected profiles before storage [17], [18].

Since it has already been validated in several missions, CAL is a good tool for validating the 2-μm lidar system [17]. The operation at two different wavelengths allows the comparison of various atmospheric features such as boundary layer height and structure and clouds with the 2-μm lidar. Besides, this lidar has two detection systems relying on two different well-established

Authorized licensed use limited to: University of North Texas. Downloaded on December 18,2020 at 12:58:59 UTC from IEEE Xplore. Restrictions apply.

TABLE I
PARAMETERS OF THE THREE LIDAR SYSTEMS FOR COMPARISON

Parameter	CAL, 532-Ch	CAL, 1064-Ch	2-μm Lidar
Transmitter;			
Wavelength	532 nm	1064 nm	2053 nm
Laser Energy	56 mJ	42 mJ	90 mJ
Repetition Rate	20 Hz	20 Hz	5 Hz
Pulse Width	15 ns	15 ns	130 ns
Beam Divergence	1.5 mrad	1.5 mrad	85 μrad
Receiver;			
Telescope Diameter	0.28 m	0.28 m	0.40 m
Field-of-View	2 mrad	2 mrad	350 μrad
Receiver Efficiency	61.4%	44.0%	58.0%
Receiver Split Factor	0.9	1	1
Detector Type	PMT	APD	HPT
Detector Part #	MH-943	C30955E	A1-a2
Digitizer Bits	14	14	12
Sampling Rate	5 MS/s	5 MS/s	5 MS/s
Default Shot Average	20	20	1

detector technologies (PMT and Si-APD), which provide an evaluation opportunity for the HPT in lidar applications. Table I summarizes the main parameters of the 2-μm lidar and the CAL systems.

A. 2-μm Lidar Transmitter

The lidar transmitter, shown in Fig. 1, consists of a 2-μm laser that was designed for CO_2 DIAL applications [19]. This 90-mJ, 140-ns, 5-Hz pulsed Ho:Tm:LuLiF oscillator is injection-seeded by continuous wave (CW) lasers to produce a tunable single-frequency spectrum of 3.4-MHz linewidth. The laser design is described in detail in another publication and is only briefly summarized here [19]. Three CW lasers are used to provide wavelength control and wavelength alternation for DIAL measurements. One CW laser, the center reference, is locked onto line center by sending most of its beam into a multipass cell containing CO_2. An electro-optic modulator and associated demodulation electronics provide a feedback signal to continuously tune the center reference laser onto line center. A second CW laser is used, the online laser, to create a frequency offset from the centerline reference. An active locking circuit on the frequency offset is generated by heterodyning a portion of the beams from the center reference and online lasers. These two beams are mixed in an evanescent wave coupler, resulting in a measurement of the difference in frequency between the two lasers. A desired frequency offset can be selected to maintain the frequency difference. A third CW laser provides the off-line wavelength. Alternation of the online and off-line lasers is accomplished with an electro-optic switch. As the pulsed laser is fired, a logic signal is generated to enable the switch to alternatively select the online and off-line CW lasers to injection-seed the next pulse of the pulsed laser. The output pulsed laser beam is then expanded (20X) and steered upward using folding mirrors and transmitted coaxially with the receiver telescope. Beam expansion limits the divergence to 85 μ-radians and reduces the transmitted intensity $(\mathrm{J/m^2})$ well below the maximum permissible exposure of 100-mJ/cm^2 for eye safety [19].

B. 2-μm Lidar Receiver

The optical schematic of the lidar receiver is shown in Fig. 1. The receiver telescope is pointing in the zenith direction. To minimize thermal effects, the lidar receiver utilizes a 40-cm diameter F/2.2 all aluminum Cassegrain telescope. The telescope FOV is set to 350 μ-radians by the inlet of the optical fiber cable. One design specification for this telescope was to achieve a small focus area of 180 μm diameter, which allows for coupling the collected radiation using a multimode fiber optic cable. The fiber optic output is collimated and focused using triplet lens design fabricated from SF11 optical glass. The optical design allows focusing of the optical radiation onto a 200-μm-diameter spot size, compatible with the HPT sensitive area. The HPT has several advantages over InGaAs pin and HgCdTe p-n 2-μm detectors, including high gain and quantum efficiency with low noise-equivalent-power (NEP). A 2-μm lidar detection system was integrated using the HPT [15]. As shown in Fig. 1, the main features of the detection system electronics include computer controlled detector bias, temperature control electronics, trans-impedance amplifier with dark current compensation, and voltage amplifier with offset and gain adjustments. Digital electronics control the setting of the detection system. The detection system is powered by rechargeable batteries (10 h operation) for noise minimization. The telescope, optics, and HPT detection system are enclosed inside an aluminum box to limit stray radiation. The detection system output was applied to a 12-bit, 5-MS/s waveform digitizer (National Instrument NI-6115). Single shot profiles were stored in the system computer (National Instruments PXI-chase) for further analysis.

III. TWO-MICROMETER BACKSCATTER LIDAR VALIDATION

On April 25, 2008, CAL and the 2-μm lidar were operated at NASA LaRC. Both systems were profiling backscattered signals from atmospheric structures from the near-field boundary layer and far-field clouds. Fig. 2 shows the false color timing diagram for the boundary layer structure using each lidar system. Data were collected for about an hour, as indicated in the horizontal axis versus altitude (up to 5 km) in the vertical axis. The false color represents the independent signal strength from each of the lidar channels as digitizer output voltage that has been range-corrected (multiplied by the square of the range). According to Fig. 2(b) and (c), measurement in the upper region of the boundary layer (above 1 km) allow for long averages due to minimal temporal variation in the atmospheric structure in that region. In such case, shot noise is minimized while emphasizing systematic noise (i.e., internal noise generated by the lidar detection system) in lidar signals. Data from the three wavelengths show a boundary layer thickness of about 2.1 km with a thin aerosol layer between 2.6 and 3.5 km. Data processing for the 532- and 1064-nm lidars included background subtraction, shot averaging, and range correction. Similar data processing was applied to the 2053-nm lidar, with a deconvolution processing before the range correction [16]. To preserve the same time span,

Authorized licensed use limited to: University of North Texas. Downloaded on December 18,2020 at 12:58:59 UTC from IEEE Xplore. Restrictions apply.

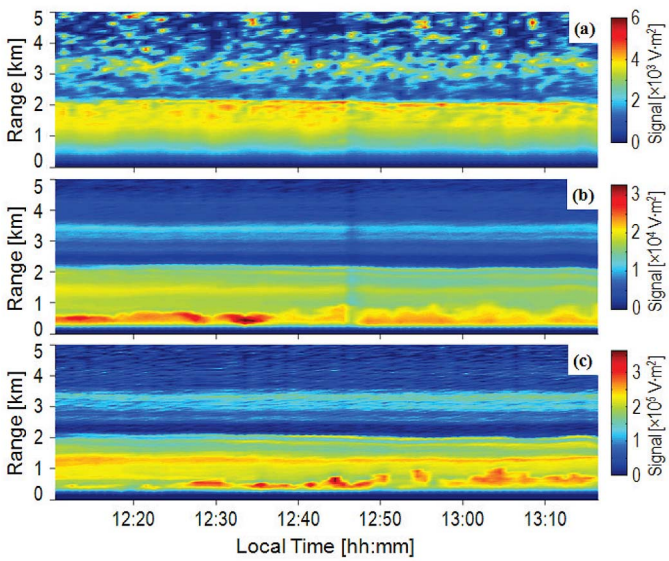

Fig. 2. False color diagrams for the near-field boundary layer profiles measured on April 25, 2008 using CAL operating at (a) 532 nm and (b) 1064 nm and the 2-μm lidar operating at (c) 2053 nm. The false color scale represents the independent signals strength from each of the lidar channels. The profiles are plotted against the measurement time in the horizontal axis and the range in the vertical axis. To preserve the same time scale, shot average of 1200 was applied to (a) and (b) and of 300 to (c).

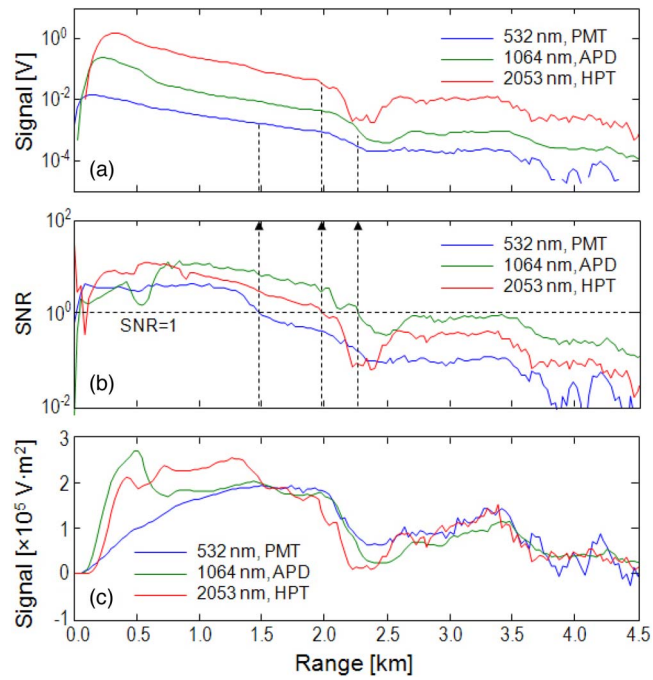

Fig. 3. (a) Lidar signal profiles at 532, 1064 and 2053 nm using a fixed 3000-shot average. (b) Corresponding SNR profiles obtained by calculating the standard deviation per range bin. System extracted NEP was obtained by the intersection with unity SNR and extracting the signals form (a) as marked by the vertical dotted lines and presented in Table II. (c) The corresponding range corrected profiles. For clarity, 532- and 1064-nm profiles were multiplied by 50 and 10, respectively.

averaging of 1200 and 300 shots were applied for the CAL and 2-μm lidar systems data, respectively.

Profiling using the 1064-nm APD, shown in Fig. 2(b), indicates best performance with respect to SNR, followed by 2053 nm using the HPT. The poor performance of the PMT at 532 nm is attributed to system optimization issues. These issues include the overlap function and the signal conditioning amplification before digitizer. To further investigate the lidar performances while operating at different wavelengths and using different detector technologies, shot-averaged signal profiles are shown in Fig. 3. The profiles in Fig. 3(a) represent the same shot average of 3000, equivalent to time spans of 2.5 and 10 min for the CAL and 2-μm lidars, respectively. The corresponding SNR, shown in Fig. 3(b), was achieved after calculating the standard deviation at each range bin [20]. The resultant range corrected profiles, shown in Fig. 3(c), clearly indicate a slower overlap function for the 532-nm lidar. Using these profiles, the "detection system NEP" (NEP_s) was extracted using the equation [16]

$$NEP_s = \left(A/G_d \cdot \sqrt{BW}\right) \cdot S|_{SNR=1} \tag{1}$$

where A is the detector area, G_d and BW are the detection system gain (in $\mathrm{V \cdot cm^2/W}$) and bandwidth, respectively, and S is the output signal at $\mathrm{SNR} = 1$. The extracted values of the NEP were compared to the detectors' NEP (NEP_d) in Table II. NEP_s represents the noise contribution of the whole detection channel including the detector and associated electronics. Ideally, the dominant noise source in a backscatter lidar system should be the detector (optical transducer). Proper system design should include negligible noise effects from the detection system electronics. In order to normalize the detector area, Table II also presents the "equivalent extracted detectivity" (D_s^*), obtained from

$$D_s^* = \frac{G_d}{S|_{SNR=1}} \cdot \sqrt{\frac{BW}{A}} \tag{2}$$

as compared to the detectors' detectivities (D_d^*). Also, to fully evaluate the HPT, data were obtained from [16] for the HPT operation results at 1532 nm.

Fig. 4 compares the individual detector and detection system detectivity results obtained from Table II with the background limited detectivity (D_{BL}^*). The background limited detectivity was calculated according to the relation [21]

$$D_{BL}^* = \lambda / \left(2 \cdot h \cdot c \cdot \sqrt{E_{BG}}\right) \tag{3}$$

where λ is the wavelength, h is Plank's constant, c is the speed of light, and E_{BG} is the photon background irradiance (in photons/s $\cdot$ cm^2). Applying Plank's blackbody radiation law, the photon background irradiance is calculated by [21]

$$E_{BG} = \int_0^{\lambda} \frac{2\pi \cdot c \cdot \sin^2(\theta/2)}{\lambda^4 \cdot [\exp(h \cdot c/\lambda \cdot k \cdot T) - 1]} \cdot d\lambda \tag{4}$$

where k is the Boltzmann's constant, T and θ are the background temperature and FOV, assumed 293 K and 180°, respectively. At 532 nm, the background detectivity is very high, indicating a wide region for detection improvement at this wavelength. This is clear from the PMT D^*, which reaches a

Authorized licensed use limited to: University of North Texas. Downloaded on December 18,2020 at 12:58:59 UTC from IEEE Xplore. Restrictions apply.

TABLE II
COMPARISON BETWEEN THE DETECTORSAND LIDAR DETECTION SYSTEMS PERFORMANCES

	PMT	APD	HPT		
		Device Performance			
Part Number	MH-943	C30955E	HPT1 (b)	HPT2 (b)	A1-b10
λ (nm)	532 nm	1064 nm	1543 nm	1543 nm	2053 nm
d (mm)	5 mm	1.5 mm	0.2 mm	0.2 mm	0.2 mm
R (A/W)	3.0×10^{6}	34.0	159.4	4.0	400.0
I_n (A/Hz$^{1/2}$)	9.5×10^{-16} (a)	2×10^{-12}	2.3×10^{-10}	3.8×10^{-11}	2.3×10^{-10}
NEP_d (W/ Hz$^{1/2}$)	3.2×10^{-22}	5.6×10^{-14}	1.4×10^{-12}	9.5×10^{-12}	5×10^{-13}
D^*_d (Jones)	1.4×10^{21}	2.4×10^{12}	1.27×10^{10}	1.87×10^{9}	3.54×10^{10}
		System Performance			
$S\|_{SNR=1}$ [mV]	1.76	0.99	6.16	27.61	34.69
$R\|_{SNR=1}$ [m]	1470	2280	2235	3690	1980
G_d [V/(W/cm^2)]	14.7×10^{6}	4750	671.4	451.7	3455
BW [MHz]	2.5	1.5	2.5	2.5	2.5
NEP_s [W/Hz$^{1/2}$]	1.48×10^{-14}	3.01×10^{-12}	1.82×10^{-12}	1.21×10^{-11}	1.99×10^{-12}
D^*_s [Jones]	2.99×10^{13}	4.42×10^{10}	9.72×10^{9}	1.46×10^{9}	8.88×10^{9}

(a) PMT noise current estimated from the Equivalent Input Noise (EIN=10-17 W) and the response time (3 nsec).
(b) Results from reference 16. Device A1-b10 was used in HPT1 of reference 16.

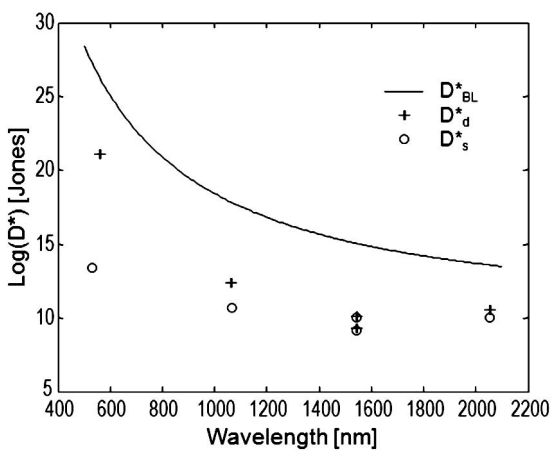

Fig. 4. Detectivity comparison between different detectors (D^*_d) operating at different wavelengths (PMT for 532 nm, APD for 1064 nm, and HPT for 1543 and 2053 nm). Also, the lidar detection systems detectivity (D^*_s) is presented and compared to the ideal background limit (D^*_{BL}).

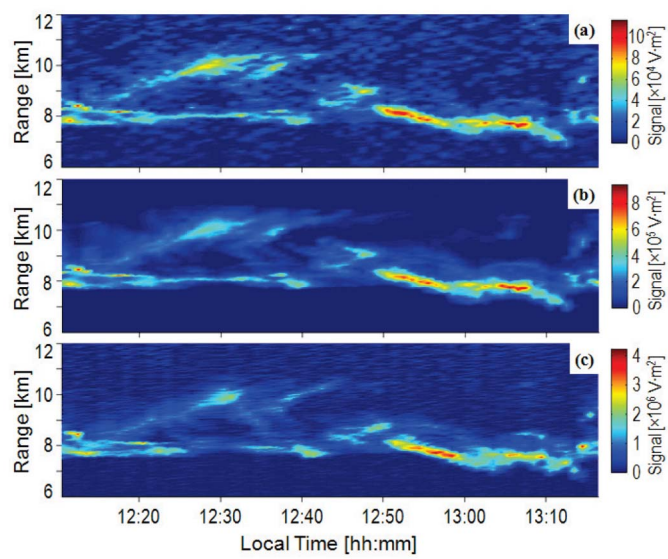

Fig. 5. False color diagrams for the far-field profiles measured on April 25, 2008 using CAL at (a) 532 nm and (b) 1064 nm and the 2-μm lidar at (c) 2053 nm. The false color represents the independent signal strength from each of the lidar channels. The profiles are plotted against the measurement time in the horizontal axis and the range in the vertical axis. To preserve the same time scale, shot average of 1200 was applied to (a) and (b) and of 300 to (c).

relatively high value. Nevertheless, the PMT-associated electronics contribute significantly to the noise, resulting in deteriorating the overall lidar performance compared to the other detection systems. Although the Si APD operates at 1064 nm, which results in relatively lower quantum efficiency, the device achieves reasonable detectivity compared to the background. Slight reduction in the overall system D^*_s indicates better system performance, compared to the PMT system D^*_s, due to the domination of the detector noise. In the case of HPT, the devices originally exhibited high noise, leading to lower restrictions on the detection electronics. This leads to negligible noise contribution from the system compared to the detector. Besides, the HPT high gain will increase the D^* further toward the background limit [6]. This is demonstrated while operating the HPT at 1532 nm. At 2053 nm, the D^* of the HPT would increase more due to higher quantum efficiency [6]. On the other hand, 2053 nm D^*_s will be reduced more than 1532 nm due to the deconvolution process [16]. Nevertheless, from Fig. 4, the 2053-nm system performance using the HPT is comparable to the 1064-nm system using the Si-APD.

Focusing on the far-field, Fig. 5 shows the lidar profiles between 6 and 12 km. Similar analysis was applied as with the near-field case. The systems are profiling a cloud structure extending from 8 to 11 km. Considering the 1064 and 2053 systems, selected sample profiles are shown in Fig. 6. In this figure, the HPT data are presented before and after the deconvolution process. This shows the recovery of the system resolution while reducing the SNR. For example, the sharp cloud feature located at 8090 m, with 60-m width, was detectable using the HPT device at 2053 nm. Statistical analysis of the data presented in Fig. 6 resulted in a correlation coefficient of 0.94 and 0.82 between the 1064 and 2053 nm before and after the deconvolution, respectively. On the other hand, the same correlation coefficient calculations were applied to the near-field profiles, presented

Authorized licensed use limited to: University of North Texas. Downloaded on December 18,2020 at 12:58:59 UTC from IEEE Xplore. Restrictions apply.

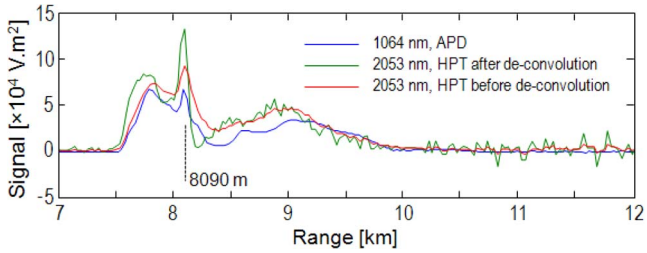

Fig. 6. Sample profile from Fig. 5 obtained at 12:19:00, showing the sensitivity of both systems to 60-m wide feature. The 2053 nm profiles are shown before and after the deconvolution process.

in Fig. 3(a), resulting in 0.77 and 0.89 between the 1064 and 2053 nm profiles before and after the deconvolution, respectively. Perfect correlation was not expected due to the differences in the aerosol scattering between the two wavelengths. The results indicates the significance of the deconvolution process to the near-field data, where faster transients occur, rather than the far-field, were relatively slower signals gradient do not require higher detection bandwidth. The deterioration of the correlation coefficient in the far-field is mainly attributed to the application of the deconvolution process only to the HPT data, but not to the APD data [16]. It should be mentioned that the near-field is the critical range for profiling atmospheric carbon dioxide.

IV. Two-Micron Lidar Operation in DIAL Mode

To validate the 2-μm lidar for atmospheric carbon dioxide measurement, the system was operated in the DIAL mode. This was achieved by switching the 2-μm laser transmitter between off-line and side-line wavelengths around the carbon dioxide R22 line. Side-line operation was selected rather than the line peak (online) to reduce the radiation absorption that limits the range measurement capability [19]. The off-line wavelength was fixed at 2053.449 nm, while the side-line was adjusted to either 2.15 or 2.80 GHz from the CO_2 R22 line center. The receiver system was unchanged and the off-line and side-line data separation was achieved by sorting odd and even data shots. On May 19, 2008, CAL and the 2-μm lidar systems were operated at NASA LaRC to monitor the atmospheric structure. Also, an *in situ* CO_2 sensor was used for comparison to the 2-μm CO_2 DIAL measurement. Fig. 7 shows the false color diagrams for both lidar systems in the 0 to 4 km range. The time spans were about 30 min for each of the side-line settings. Data analysis included the same steps discussed before. For the 2-μm lidar, the shot average was reduced to 150 shots to account for the double pulsing (side-line and off-line), thus maintaining the same time interval. The figure clearly indicates the reduction of the side-line signals compared to the off-line. The 2.15 GHz side-line setting has stronger absorption as compared to the 2.80 GHz, resulting in weaker signals as seen in the figure. This was expected due to stronger absorption closer to the R22 peak, as shown in Fig. 8.

Fig. 8 shows both carbon dioxide and water vapor absorption spectrum near the R22 line. For carbon dioxide side-line and off-line absorption cross-section calculations ($\sigma_{\rm on}$ and $\sigma_{\rm off}$, respectively), the R22 line and the strongest 59 neighboring lines were fitted using Voigt profile [22]. Line parameters including line center location and intensity, air-broadened and self-broadened half-width-half-maximum (HWHM), lower state energy, coefficient of temperature dependence, and air-broadened pressure shift were obtained from the HITRAN database and literature [23]–[26]. Corrections to the line parameters included the pressure-shift of the line position, temperature correction of the line intensity, and temperature and pressure correction for the line HWHM [26]. The temperature correction of the line intensity was applied after calculating the total internal partition function [26], [27]. The lines HWHM were calculated, assuming a CO_2 partial pressure corresponding to a fixed mixing ratio of 380 ppm [26]. For water vapor cross sections, similar analysis was applied using parameters obtained from HITRAN for 88 lines around the CO_2 R22 line [23]. The water vapor partial pressure was calculated from relative

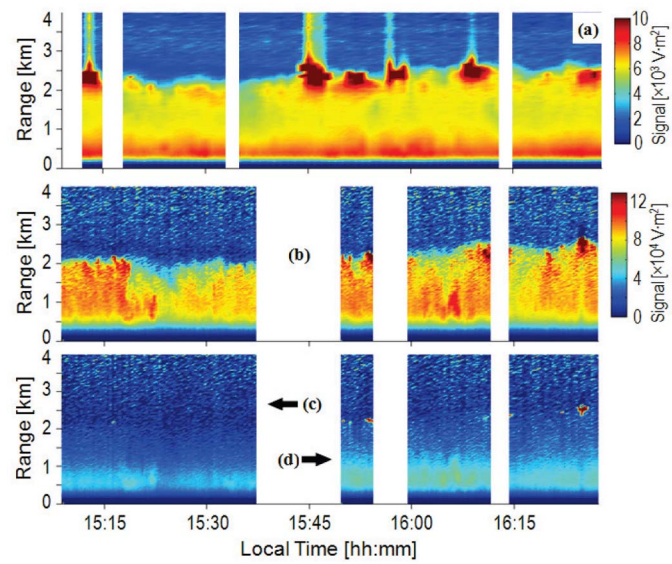

Fig. 7. False color diagrams for the near-field boundary layer profiles measured on May 19, 2008 using CAL operating at (a) 1064 nm and the 2-μm lidar operating in DIAL mode at (b) off-line 2053.449 nm and (c) 2.15 GHz side-line and (d) 2.80 GHz side-line. Time discontinuity in the data is attributed to system adjustments.

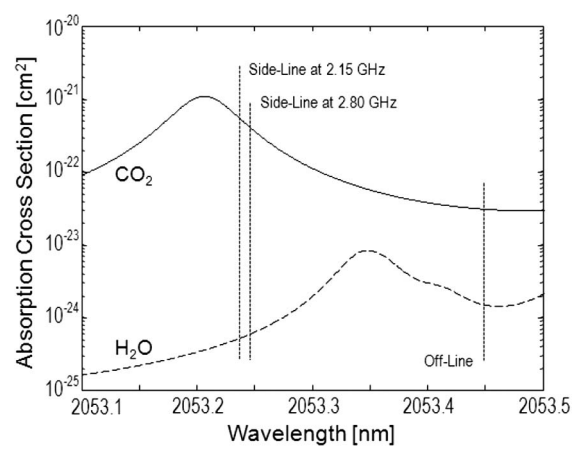

Fig. 8. Carbon dioxide and water vapor absorption cross-section spectra around the CO_2 R22 absorption line. Spectral calculation was obtained using Voigt line profile with 1×10^{-3} cm^{-1} resolution, assuming atmospheric pressure of 1.01×10^5 Pascal, temperature of 296 K, and relative humidity of 10%. Dotted vertical lines point the selected wavelength for DIAL operation.

Authorized licensed use limited to: University of North Texas. Downloaded on December 18,2020 at 12:58:59 UTC from IEEE Xplore. Restrictions apply.

humidity and temperature profiles [28]. According to Fig. 8, it is observed that the CO_2 measurement sensitivity will be affected by the water vapor due to the off-line and side-lines locations. The effect of water vapor arises in the dry air number density calculation and its interference to the CO_2 DIAL calculation. This could produce an error as high as 10% to the boundary layer carbon dioxide mixing ratio measurements at the selected wavelengths. For example, assuming a standard temperature of 296 K, pressure of 101 kPascal, and 10% relative humidity, the carbon dioxide and water vapor differential cross sections between the 2.15 GHz side-line and off-line will be 5.6×10^{-22} and 9.8×10^{-25} cm^2, respectively. With 380 and 2761.6 ppm carbon dioxide and water vapor mixing ratios, respectively, the resultant differential absorption coefficients are 5.2×10^{-6} and 6.6×10^{-8} cm^{-1}. This indicates a 1.3% deviation in carbon dioxide estimates between including and excluding the water vapor effect. Without water vapor correction, the deviation will increase to 11% if the relative humidity increases to 80%. Proper selection of the side-line and off-line wavelengths could eliminate such an effect by minimizing the water vapor interference. Upon availability of transmitter technology, this could be easily achieved by switching to the carbon dioxide R30 absorption line [8].

In situ CO_2 measurements were made using a modified LI-COR model 6252 nondispersive infrared (NDIR) gas analyzer-based sampling system [29], [30]. This dual cell instrument achieves high precision by measuring the differential absorption between sample air and a calibrated reference gas that is traceable to the World Metrological Organization primary calibration standards maintained at the National Oceanic and Atmospheric Administration, Climate Monitoring and Diagnostics Laboratory in Boulder, CO. During ambient sampling, air was continuously drawn through the 5.5-m-high inlet, a permeable membrane dryer to remove water vapor, the LI-COR analyzer, and then through the diaphragm pump. Frequent but short calibrations with well-documented and stable calibration gases, critical to achieving both high precision and accuracy, were accomplished by periodically (~20 min) flowing calibration gas through the instrument's sample cell. The system was operated at a constant mass flow rate (500 cm^3 min^{-1}) and pressure (250 torr), and had a precision of $\leq$ 0.1 ppm and accuracy of $\pm$0.25 ppm for 1-Hz sampling rates [29], [30].

Fig. 9 shows a comparison between the *in situ* and the DIAL CO_2 measurements obtained using the 2.15 and 2.80 GHz side-lines. The measurements, summarized in Table III, were obtained simultaneously in the afternoon when the carbon dioxide is well mixed in the boundary layer. This is due to stable bioactivities associated with well mixing convection currents. Thus, the gas concentration would exhibit minimal variation through different altitudes up to the boundary layer edge. The DIAL data were analyzed using 100-shot average (40 s temporal resolution) and 20-iteration deconvolution. Due to interference from the window reflection, the first two samples were eliminated. Then, 9-point temporal smoothing average were followed by 9-point range running average were applied to the side-line and off-line records before power ratio calculations. This results in 270 m spatial resolution (range cell). Generally, assuming an original backscatter profile with

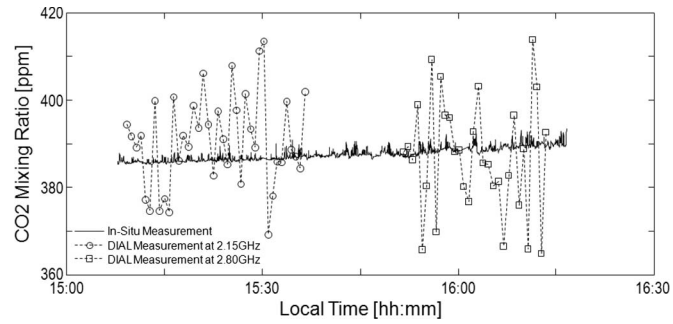

Fig. 9. May 19, 2008 comparison between carbon dioxide *in situ* and DIAL measurements. DIAL was obtained at 2.15 GHz then 2.80 GHz away from R22 CO_2 line peak. DIAL data analysis included 100 shot average (40 s), 20 iteration deconvolution and 270 m spatial resolution. After calculating the carbon dioxide mixing ratio, the average between 465 to 735 m was taken.

TABLE III
COMPARISON BETWEEN THE CARBON DIOXIDE MIXING RATIO MEASUREMENTS USING THE *IN SITU*, $N_{In-Situ}$, AND THE DIAL TECHNIQUE, N_{DIAL}, PRESENTED IN FIG. 9. THE DIAL WAS PERFORMED AT THE TWO SIDE LINES WAVELENGTHS, SHIFTED BY $\delta\upsilon_{\mathrm{side-line}}$ FROM THE R22 LINE CENTER

$\delta\upsilon_{\text{side-line}}$ [GHz]	2.15	2.80
σ_{on} [cm^2] a)	5.43×10^{-22}	4.05×10^{-22}
σ_{off} [cm^2] b)	3.03×10^{-23}	3.03×10^{-23}
N_{DIAL} c)	390.8	387.0
ΔN_{DIAL}	10.6	13.0
$\Delta N_{DIAL}/N_{DIAL}$	2.7%	3.3%
$N_{In\text{-}Situ}$	386.4	388.9
$\Delta N_{In\text{-}Situ}$	0.6	1.0
$\Delta N_{In\text{-}Situ}/N_{In\text{-}Situ}$	0.1%	0.2%

a) Assumed fixed pressure and temperature of 1.01×10^5 Pa and 296 K, respectively.
b) Assumed fixed Off-line location at 2053.449 cm^{-1}.
c) Using the temperature and pressure and applying ideal gas law for air

M samples, the N-point smoothing (or walking) average is obtained by replacing each data point $y(i)$ by a smoothed point $y_s(i)$, given by

$$y_s(j) = \frac{1}{N} \cdot \sum_{i=j+(1-N)/2}^{i=j+(N-1)/2} y(i) \tag{5}$$

where i and j are the sample indices of the original and averaged profiles, respectively. In such process, N has to be an odd number and the resultant profile will be clipped relative to the original profile by $(N-1)/2$ points at both ends. On the other hand, assuming the same original profile, the N-point running average replaces each data point by an averaged point, $y_r(j)$ given by

$$y_r(j) = \frac{1}{N} \cdot \sum_{i=N\cdot(j-1)+1}^{i=j\cdot N} y(i). \tag{6}$$

In such case, the profile temporal resolution will be reduced by a factor equals to N. Wallops Island metrological data were used to correct the lidar results for temperature and pressure effects on cross-section calculations. Besides, relative humidity profiles were used to estimate the water vapor number density. After applying the DIAL equation for calculating the carbon dioxide number density, dry air number density was used to

Authorized licensed use limited to: University of North Texas. Downloaded on December 18,2020 at 12:58:59 UTC from IEEE Xplore. Restrictions apply.

calculate the gas mixing ratio. Finally, an average between 465 and 735 m altitude was taken. This procedure was applied for both measurements at 2.15 and 2.80 GHz side-lines as presented in Fig. 9. The results demonstrate the capability of the 2-μm lidar system to capture atmospheric CO_2 using the DIAL technique. The lack of high resolution metrological data (temporal and special) at the measurement location prevent the comparison of the fine-scale features in the DIAL data with *in situ* measurements.

V. Conclusion

A 2-μm backscatter lidar system has been developed at NASA Langley Research Center. The system utilizes advanced technologies in the form of a tunable 2-μm pulsed laser and an IR phototransistor for the lidar transmitter and receiver, respectively. Lidar aerosol backscatter profiles were compared to CAL for validation. This allowed comparison of different lidar systems operating at 532, 1064, and 2053 nm wavelengths using PMT, APD, and hetero junction phototransistor detection technologies, respectively. To achieve this comparison the detectivity of the lidar detection systems were extracted from the data and compared to the individual detectors, as well as the background limited detectivity. Comparison indicated the significance of the detection system electronics optimization so that the detector becomes the dominant noise source in the system. The heterojunction phototransistor showed acceptable performance for 2-μm lidar applications.

Using the differential absorption lidar technique, the 2-μm lidar system was able to quantify atmospheric carbon dioxide concentrations in the boundary layer. DIAL measurements resulted in mean values of the gas mixing ratio of 390.8 and 387.0 ppm using 2.15- and 2.80-GHz side-lines, respectively. The mixing ratios were confirmed by *in situ* measurements with 3% uncertainty. Availability of high spatial and temporal resolution metrological data appears to limit the capability of the system while operating at the selected wavelengths. An optimum side-line and off-line wavelength selection would compensate for such effect reducing the measurement error. Although these limitations prevent comparison of fine *in situ* scale features, this 2-μm lidar demonstrated a promising solution for atmospheric carbon dioxide profiling. Further range resolved validation experiments must be conducted to quantify the measurements for a future state-of-the-art CO_2 profiling system. Further system improvement includes reduction of water vapor interference, implementing daytime filter, and locking the off-line wavelength. Operating on the carbon dioxide R30 line potentially increases the system sensitivity while reducing the water vapor interference close to zero. Applying a low bandwidth filter could significantly reduce the background leading to further noise reduction. Finally, locking the off-line position increases the accuracy of the cross-section calculation.

Acknowledgment

The authors would like to thank S. Vay for supplying the CO_2 *in situ* instrumentation, S. Burton for supplying metrological records, B. Barnes for assisting in digitizer setup, and M. Kavaya for technical discussion.

References

[1] R. Measures, *Laser Remote Sensing: Fundamentals and Applications*. New York: Wiley, 1984.

[2] N. Sugimoto, N. Sims, K. Chan, and D. Killinger, "Eye-safe 2.1 μm Ho lidar for measuring atmospheric density profiles," *Opt. Lett.*, vol. 15, no. 6, pp. 302–304, Mar. 1990.

[3] P. Ambrico, A. Amodeo, P. Girolamo, and N. Spinelli, "Sensitivity analysis of differential absorption lidar measurements in the mid-infrared region," *Appl. Opt.*, vol. 39, no. 36, pp. 6847–6865, Dec. 2000.

[4] S. Cha, K. Chan, and D. Killinger, "Tunable 2.1-μm Ho lidar for simultaneous range-resolved measurements of atmospheric water vapor and aerosol backscatter profiles," *Appl. Opt.*, vol. 30, no. 27, pp. 3938–3943, Sep. 1991.

[5] J. Yu, B. Trieu, E. Modlin, U. Singh, M. Kavaya, S. Chen, Y. Bai, P. J. Petzar, and M. Petros, "1 J/pulse Q-switched 2 μm solid-state laser," *Opt. Lett.*, vol. 31, no. 4, pp. 462–464, Feb. 2006.

[6] T. Refaat, N. Abedin, O. Sulima, S. Ismail, and U. Singh, "AlGaAsSb/InGaAsSb phototransistors for 2- μm remote sensing applications," *Opt. Eng.*, vol. 43, no. 7, pp. 1647–1650, Jul. 2004.

[7] S. Ismail, G. Koch, N. Abedin, T. Refaat, M. Rubio, and U. Singh, "Development of laser, detector, and receiver systems for an atmospheric CO_2 lidar profiling system," in *Proc. IEEE Aerosp. Conf.*, Big Sky, MT, Mar. 2008, pp. 1–7.

[8] G. Ehret, C. Kiemle, M. Wirth, A. Amediek, A. Fix, and S. Houweling, "Space-borne remote sensing of CO_2, CH_4, and N_2O by integrated path differential absorption lidar: A sensitivity analysis," *Appl. Phys. B*, vol. 90, no. 3/4, pp. 593–608, Mar. 2008.

[9] D. Sakaizawa, C. Nagasawa, T. Nagai, M. Abo, Y. Shibata, M. Nakazato, and T. Sakai, "Development of a 1.6 μm differential absorption lidar with a quasi-phase-matching optical parametric oscillator and photon-counting detector for the vertical CO_2 profile," *Appl. Opt.*, vol. 48, no. 4, pp. 748–757, Feb. 2009.

[10] M. Uchiumi, N. Vasa, M. Fujiwara, S. Yokoyama, M. Maeda, and O. Uchino, "Development of DIAL for CO_2 and CH_4 in the atmosphere," *Proc. SPIE*, vol. 4893, pp. 141–149, 2003.

[11] T. Hamazaki, Y. Kaneko, A. Kuze, and K. Kondo, "Sensor system for Greenhouse Gas Observing Satellite (GOSAT)," *Proc. SPIE*, vol. 5543, pp. 275–282, 2004.

[12] D. Crisp, R. Atlas, F. Breon, L. Brown, J. Burrows, P. Ciais, B. J. Connor, S. C. Doney, I. Y. Fung, D. J. Jacob, C. E. Miller, D. O'Brien, S. Pawson, J. T. Randerson, P. Rayner, R. J. Salawitch, S. P. Sander, B. Sen, G. L. Stephens, P. P. Tans, G. C. Toon, P. O. Wennberg, S. C. Wofsy, Y. L. Yung, Z. Kuang, B. Chudasama, G. Sprague, B. Weiss, R. Pollock, D. Kenyon, and S. Schroll, "The Orbiting Carbon Observatory (OCO) mission," *Adv. Space Res.*, vol. 34, no. 4, pp. 700–709, 2004.

[13] G. Koch, B. Barnes, M. Petros, J. Beyon, F. Amzajerdian, J. Yu, R. E. Davis, S. Ismail, S. Vay, M. J. Kavaya, and U. N. Singh, "Coherent differential absorption lidar measurements of CO_2," *Appl. Opt.*, vol. 43, no. 26, pp. 5092–5099, Sep. 2004.

[14] F. Gibert, P. Flamant, D. Bruneau, and C. Loth, "Two-micrometer heterodyne differential absorption lidar measurements of the atmospheric CO_2 mixing ratio in the boundary layer," *Appl. Opt.*, vol. 45, no. 18, pp. 4448–4458, Jun. 2006.

[15] T. Refaat, S. Ismail, T. Mack, N. Abedin, S. Mayor, S. Spuler, and U. Singh, "Infrared phototransistor validation for atmospheric remote sensing application using the Raman-shifted eye-safe aerosol lidar," *Opt. Eng.*, vol. 46, p. 086001, 2007.

[16] T. Refaat, S. Ismail, N. Abedin, S. Spuler, S. Mayor, and U. Singh, "Lidar backscatter signal recovery from phototransistor systematic effect by deconvolution," *Appl. Opt.*, vol. 47, no. 29, pp. 5281–5295, Oct. 2008.

[17] R. De Young, W. Grant, and K. Severance, "Aerosol transport in the California Central Valley observed by airborne lidar," *Environ. Sci. Technol.*, vol. 39, no. 21, pp. 8351–8357, Nov. 2005.

[18] C. Gili and R. De Young, "A compact efficient lidar receiver for measuring atmospheric aerosols," NASA, Washington, DC, NASA/TP-2006-213950, 2006.

[19] G. Koch, J. Beyon, F. Gibert, B. Barnes, S. Ismail, M. Petros, P. J. Petzar, J. Yu, E. A. Modlin, K. J. Davis, and U. N. Singh, "Side-line tunable laser transmitter for differential absorption lidar measurement of CO_2: Design and application to atmospheric measurements," *Appl. Opt.*, vol. 47, no. 7, pp. 944–956, Mar. 2008.

[20] L. Fiorani and E. Durieux, "Comparison among error calculations in differential absorption lidar measurements," *Opt. Laser Technol.*, vol. 33, no. 6, pp. 371–377, Sep. 2001.

[21] E. Dereniak and D. Crowe, *Optical Radiation Detectors*. New York: Wiley, 1991, ser. Wiley Series in Applied Optics.

Authorized licensed use limited to: University of North Texas. Downloaded on December 18,2020 at 12:58:59 UTC from IEEE Xplore. Restrictions apply.

[22] C. Young, "Calculation of the absorption coefficient for line with combined Doppler and Lorentz broadening," *J. Quant. Spectrosc. Radiat. Transf.*, vol. 5, no. 3, pp. 549–552, May/Jun. 1965.
[23] L. Regalia-Jarlot, V. Zeninari, B. Parvitte, A. Grossel, X. Thomas, P. von der Heyden, and G. Durry, "A complete study of the line intensities of four bands of CO_2 around 1.6 and 2.0 μm: A comparison between Fourier transform and diode laser measurements," *J. Quant. Spectrosc. Radiat. Transf.*, vol. 101, no. 2, pp. 325–338, Sep. 2006.
[24] R. Toth, L. Brown, C. Miller, V. Devi, and D. Benner, "Line strengths of $^{12}C^{16}O_2$: 4550–7000 cm^{-1}," *J. Mol. Spectrosc.*, vol. 239, no. 2, pp. 221–242, Oct. 2006.
[25] R. Toth, C. Miller, V. Devi, D. Benner, and L. Brown, "Air-broadened halfwidth and pressure shift coefficients of $^{12}C^{16}O_2$ bands: 4750–7000 cm^{-1}," *J. Mol. Spectrosc.*, vol. 246, no. 2, pp. 133–157, Dec. 2007.
[26] L. S. Rothman, C. Rinsland, A. Goldman, S. Massie, D. Edwards, J.-M. Flaud, A. Perrin, C. Camy-Peyret, V. Dana, J.-Y. Mandin, J. Schroeder, A. McCann, R. R. Gamache, R. B. Wattson, K. Yoshino, K. V. Chance, K. W. Jucks, L. R. Brown, V. Nemtchinov, and P. Varanasi, "The HITRAN molecular spectroscopic database and HAWKS (HITRAN atmospheric workstation): 1996 edition," *J. Quant. Spectrosc. Radiat. Transf.*, vol. 60, no. 5, pp. 665–710, Nov. 1998.
[27] R. Gamache, S. Kennedy, R. Hawkins, and L. Rothman, "Total internal partition sums for molecules in the terrestrial atmosphere," *J. Mol. Struct.*, vol. 517/518, pp. 407–425, Feb. 2000.
[28] F. Murray, "On the computation of saturation vapor pressure," *J. Appl. Meteorol.*, vol. 6, no. 1, pp. 203–204, Feb. 1967.
[29] Y. Choi, S. Vay, K. Vadrevu, A. Soja, J. Woo, S. R. Nolf, G. W. Sachse, G. S. Diskin, D. R. Blake, N. J. Blake, H. B. Singh, M. A. Avery, A. Fried, L. Pfister, and H. E. Fuelberg, "Characteristics of the atmospheric CO_2 signal as observed over the conterminous United States during INTEX-NA," *J. Geophys. Res.*, vol. 113, no. D7, p. D07 301, 2008.
[30] S. Vay, J. Woo, B. Anderson, K. L. Thornhill, D. R. Blake, D. J. Westberg, C. M. Kiley, M. A. Avery, G. W. Sachse, D. G. Streets, Y. Tsutsumi, and S. R. Nolf, "Influence of regional-scale anthropogenic emissions on CO_2 distributions over the western North Pacific," *J. Geophys. Res.-Atmos.*, vol. 108, no. D20, p. 8801, 2003.

Tamer F. Refaat (M'00) received the B.S. (with honors) and M.S. degrees in electrical engineering from Alexandria University, Alexandria, Egypt, in 1991 and 1995, respectively. He received the Ph.D. degree from Old Dominion University, Norfolk, VA, in 2000.

He is currently a Senior Research Scientist with the Applied Research Center, Old Dominion University. He is also currently with the National Aeronautics and Space Administration Langley Research Center, Hampton, VA. His research interests include radiation detectors and its application to the lidar and differential absorption lidar systems for atmospheric remote sensing.

Dr. Refaat is a member of SPIE.

Syed Ismail received the Ph.D. degree in space physics from the University of Calgary, Calgary, Canada, in 1979.

He is currently a Senior Research Scientist in the Science Directorate with the National Aeronautics and Space Administration (NASA) Langley Research Center, Hampton, VA. He is internationally recognized for his research in differential absorption lidars for the atmospheric monitoring of ozone, water vapor, carbon dioxide, and aerosols.

Dr. Ismail is the recipient of NASA's Exceptional Achievement and Exceptional Service Medals in 1996 and 2009, respectively. He is a member of the American Geophysical Union and the American Meteorological Society.

Grady J. Koch received the B.S. degree in electrical engineering from Virginia Tech, Blacksburg, VA, in 1991, the M.S. degree in electrical engineering from the University of Illinois at Urbana-Champaign, Urbana, IL, in 1995, and the Ph.D. degree in electrical engineering from Old Dominion University, Norfolk, VA, in 2001.

He is currently an Aerospace Technologist with the National Aeronautics and Space Administration Langley Research Center, Hampton, VA. His research interests include coherent lidar, differential absorption lidar, solid-state lasers, and diode lasers.

Manuel Rubio, photograph and biography not available at the time of publication.

Terry L. Mack, photograph and biography not available at the time of publication.

Anthony Notari, photograph and biography not available at the time of publication.

James E. Collins, photograph and biography not available at the time of publication.

Jasper Lewis, photograph and biography not available at the time of publication.

Russell De Young, photograph and biography not available at the time of publication.

Yonghoon Choi, photograph and biography not available at the time of publication.

M. Nurul Abedin (M'00) received the Ph.D. degree in solid state physics from Rensselaer Polytechnic Institute, Troy, NY, in 1989.

He is currently a Lead Electro-Optics Sensor Technologist of the Remote Sensing Flight Systems Branch with the National Aeronautics and Space Administration Langley Research Center, Hampton, VA. His research interests include radiation detectors and active and passive remote sensing for Earth science and planetary exploration.

Dr. Abedin is a member of the Optical Society of America and SPIE.

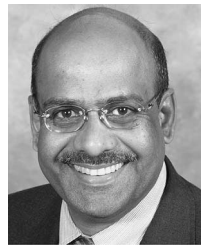

Upendra N. Singh received the Ph.D. degree in physics from the University of Pierre and Marie Curie, Paris, France, in 1985.

He is currently the Chief Technologist at Systems Engineering Competency with the National Aeronautics and Space Administration Langley Research Center, Hampton, VA. He is an internationally recognized expert on active optical remote sensing.

Dr. Singh is a Fellow and active member of SPIE and the Optical Society of America. He is a member of the SPIE Board of Directors (2008–2011).

Authorized licensed use limited to: University of North Texas. Downloaded on December 18,2020 at 12:58:59 UTC from IEEE Xplore. Restrictions apply.